Validation of Landsat 7/ETM+ thermal band calibration and atmospheric correction with ground-based measurements

César Coll*[a], Joan M. Galve[a], Juan M. Sánchez[a,b], and Vicente Caselles[a]

[a]Department of Earth Physics and Thermodynamics, Faculty of Physics, University of Valencia. 50, Dr. Moliner. 46100 Burjassot, SPAIN.

[b]Department of Applied Physics, University of Castilla-La Mancha. Avenida de España. 02071 Albacete, SPAIN

* Corresponding author. Email: cesar.coll@uv.es

ABSTRACT

Ground-based measurements of land surface temperature (LST) performed in a homogeneous site of rice crops close to Valencia, Spain were used for the validation of the calibration and the atmospheric correction of the Landsat 7 Enhanced Thematic Mapper+ (ETM+) thermal band. Atmospheric radiosondes were launched at the test site around the satellite overpasses. Field emissivity measurements of the near full-vegetated rice crops were also performed. Seven concurrences of Landsat 7 and ground data were obtained in July and August 2004-2007. The ground measurements were used with the MODTRAN 4 radiative transfer model to simulate at-sensor radiances and brightness temperatures, which were compared with calibrated ETM+ observations over the test site. For the cases analyzed here, differences between simulated and ETM+ brightness temperatures show average bias of 0.6 K and root mean square difference (rmsd) of ±0.8 K. The ground-based measurements were also used for the validation of LSTs derived from ETM+ at-sensor radiances with atmospheric correction calculated from: (1) the local radiosonde profiles, and (2) the operational atmospheric correction tool available at http://atmcorr.gsfc.nasa.gov. For the first case, the differences

between the ground and satellite LSTs ranged from -0.6 to 1.4 K, with mean bias of 0.7 K and rmsd=±1.0 K. For the second case, differences ranged between -1.8 and 1.3 K, with zero average bias and rmsd=±1.1 K. Although the validation cases are few and limited to one landcover at morning and summer, results show the good LST accuracy that can be achieved with ETM+ thermal data.

I. INTRODUCTION

Landsat satellites have been providing multispectral global observations of the Earth surface at high spatial resolution since 1972. Landsat 5 (launched in 1984) and Landsat 7 (launched in 1999) are still operational and continue to provide useful measurements with the Thematic Mapper (TM) and the Enhanced Thematic Mapper+ (ETM+) instruments, respectively. Both TM and ETM+ are quite similar, including a band in the thermal infrared (TIR) region (band 6, 10.45-12.42 μm for TM and 10.31-12.36 μm for ETM+) with spatial resolution of 120 m and 60 m, respectively. The thermal band is calibrated on-board using a black-body cavity as a hot target and a highly emissive shutter at instrument ambient temperature [1]. Thermal data are provided as calibrated at-sensor (top-of-atmosphere) radiances that can be converted to equivalent brightness temperatures, with noise equivalent temperature difference <0.3 K [2].

The on-board calibration of the TM and ETM+ thermal bands has been continuously monitored using lakes as vicarious calibration targets since 1999. Early results were presented in [1] and [2] showed a warm bias of 0.31 $Wm^{-2}sr^{-1}\mu m^{-1}$ (3 K at 300 K) in the on-board calibration of ETM+, which was subsequently corrected at the end of 2000. Variable bias in TM calibration was observed between 1999 and 2003 [3]. Recently, the TM thermal band calibration was updated to correct for a constant cold bias of 0.092 $Wm^{-2}sr^{-1}\mu m^{-1}$ (0.7 K at 300 K) based on vicarious calibration results from 1999 to 2007 [4]. According to analogous vicarious calibration over lakes in 1999-2007, the ETM+ thermal band appears to be stable and calibrated within ±0.6 K after the correction of the offset error in late 2000 mentioned above [5].

Despite the Landsat archive constitutes an unmatched record of TIR remote sensing data in terms of spatial resolution, global coverage and time span, the use of Landsat thermal bands

has been less than the use of reflective bands. One reason may be that the Landsat system does not provide an operational land surface temperature (LST) product because of the limitation of the single thermal band to correct for atmospheric and emissivity effects. In order to retrieve LST from at-sensor radiances, atmospheric profiles of temperature and water vapor measured concurrently to the satellite overpass are necessary as inputs of a radiative transfer code, together with surface emissivity data. A web-based atmospheric correction tool (http://atmcorr.gsfc.nasa.gov) has been developed for TM and ETM+ thermal data [6]. It uses atmospheric profiles from the National Center for Environmental Prediction (NCEP) interpolated to a particular location, date and time and the MODTRAN 4 code [7]. The user can apply the calculated atmospheric parameters to a given scene and, assuming an emissivity value, retrieve the LST for the area of interest.

Another reason for the light use of ETM+ thermal data could be the failure in the scan line corrector (SLC) that occurred in 2003. It results in gaps and overlaps between successive scans, and thus reduces the coverage of the scene from none at the center of the scan to 14 pixels at the edge of the scan [8]. The Landsat 7 ETM+ continues to acquire image data in the "SLC-off" mode with the same high radiometric and geometric quality as data collected prior to the SLC failure.

The objective of this paper is to contribute to the vicarious calibration of the ETM+ thermal band using ground measurements performed over a homogeneous area of rice fields in Valencia, Spain during 2004-2007. The ground data was also used for the validation of the web-based atmospheric correction tool mentioned above. The Valencia test site has been used in previous studies, with its thermal homogeneity being assessed at different spatial scales [9-13]. For the present work, we used ground LST measurements and atmospheric radiosonde

profiles concurrent to seven Landsat 7 overpasses. Field emissivity measurements of the rice crops were also performed.

The paper follows with the description of the experimental data and methods used in the study, including the satellite data, the ground LSTs, the radiosonde profiles and radiative transfer calculations. The atmospheric correction tool [6] is also detailed in this section. Section III shows and discusses the results on the ETM+ thermal band calibration and the atmospheric correction tool. Section IV summarizes the main conclusions of the study.

II. MATERIALS AND METHODS

A. ETM+ data

Seven daytime Landsat 7 scenes were acquired over the test site in July and August 2004-2007 (see Table I). Scenes were downloaded from the United States Geological Survey EROS Data Center. Landsat thermal band data are given as digital numbers (DN) that are calibrated to at-sensor radiances (L_{sen}) as

$$L_{sen} = a(DN-1) \quad (1)$$

with a=0.067087 $Wm^{-2}sr^{-1}\mu m^{-1}$ for the low gain mode [2]. The brightness temperature, T_b, is obtained from the at-sensor radiance as

$$T_b = \frac{k_2}{\ln\left(\frac{k_1}{L_{sen}} + 1\right)} \quad (2)$$

with k_1=666.09 $Wm^{-2}sr^{-1}\mu m^{-1}$ and k_2=1282.7 K. A variation of 1 DN corresponds to a T_b variation of 0.5 K at 300 K. According to [2], the accuracy of the thermal band calibration is within ±0.6 K.

The processing levels of the scenes were either L1G providing systematic radiometric and geometric accuracy from data collected from the sensor and spacecraft, or L1T providing systematic radiometric and geographic accuracy using ground control points and digital elevation model as well. In both cases, the scenes were geo-referenced with sufficient accuracy to identify correctly the pixels corresponding to the test site. The coordinates of the site were 0º17'43"W, 39º15'01"N in 2004, and 0º18'28"W, 39º15'54"N in 2005-2007. We checked that the area around the test site was cloud-free by visual inspection of the reflective and thermal bands.

All scenes were affected by the failure in the scan line corrector (SLC-off mode) occurred in 2003, so part of the data in the scenes were lost. Fortunately, the area corresponding to the test site was successfully imaged for most of the scenes. For the other cases, we used the data for the valid pixels closest to the test site. This is possible due to the high thermal homogeneity of the rice field area. It was assessed by comparing the brightness temperature for the pixel closest to the test site with the mean brightness temperature for arrays of 3×3, 5×5 and 11×11 pixels centered on the site. Differences ranged between -0.5 and 0.7 K for the seven cases studied. We also calculated the standard deviation of the brightness temperatures in the pixel arrays, yielding values from 0.25 to 0.5 K. These results are close to those given in [9-11] for ASTER TIR data (90 m resolution) over the same site, and show the thermal homogeneity of the test site. The brightness temperatures for the valid pixel closest to the site are shown in the last column of Table I.

B. Ground LST measurements

Ground measurements of LST were performed at the Valencia site concurrently with Landsat 7 overpasses for the seven cases of Table I. In July and August, rice crops have nearly full

cover and are well irrigated. It makes the site highly homogeneous in terms of both surface temperature and emissivity, thus easing the radiometric measurement of LST. Three TIR radiometers were used, including two CIMEL CE 312-1 with four bands (8-13 μm, 11.5-12.5 μm, 10.5-11.5 μm and 8.2-9.2 μm), and one CIMEL CE 312-2 with six bands (8-13 μm, 8.1-8.5 μm, 8.5-8.9 μm, 8.9-9.3 μm, 10.3-11.0 μm, and 11.0-11.7 μm). The CE 312 radiometers are self-calibrated instruments allowing compensation for the radiance of the detector's cavity [14]. Additionally, the instruments were calibrated against a reference blackbody before and after each measurement day and intercompared in the field, showing absolute accuracies of 0.1-0.2 K in all bands.

Ground measurements were only performed when the sky was apparently cloud-free over the site. Moreover, we measured the downwelling sky radiance from which the equivalent temperature was calculated, yielding very low values (between -30 and -50 ºC in the 10.5-11.5 μm band) for the cases studied here.

Radiometers were placed on the rice fields at spots 50 m apart and carried back and forth along transects of 50 m in length, looking at the surface at angles close to nadir. The field of view of the radiometers was >30 cm on the crop surface. Temperatures were taken at a rate of 5-10 measurements per minute, covering a distance of 30-50 m per minute, depending on the instrument. We selected the ground temperatures measured within three minutes centered at the satellite overpass time, which were averaged. The standard deviation of the ground temperatures was calculated as a measure of the spatial and temporal variability of LST in the test site (typically ≤0.5 K). The three-minute window was adopted as a compromise between sufficient sampling (more than 20 point LST measurements per radiometer) and not introducing too much temporal variability.

Radiometric temperatures were corrected for emissivity effects, including the reflection of the sky irradiance. Surface emissivity was measured in the field using the box method [15] for the four channels of the CE 312-1 radiometers each year of campaign. We made typically 30 measurements for each channel at 3 different spots on the rice fields each year. Results show high emissivity values with low spatial, temporal and spectral variation within 8-13 μm (values between 0.980 and 0.985 with uncertainty <0.005 for the four CE 312-1 bands, [11]). For the ETM+ thermal band, we can take the mean value of the measurements at the 10.5-11.5 μm and 11.5-12.5 μm bands (ε=0.983±0.005). The sky irradiance was estimated as π times the downwelling atmospheric radiance at an angle of 53º from nadir as measured in the field with the CE312 radiometers concurrent to the temperature transects [9].

Together with the average in situ LST, we estimated the total LST uncertainty, which includes the calibration error of the ground radiometers, the emissivity correction error (~0.2 K for uncertainty of 0.005 in the measured emissivity) and the LST variability. Table II lists the ground LSTs (T_g) and uncertainties for the cases of Table I.

C. Local radiosonde profiles and radiative transfer calculations

Vaisala RS80 radiosondes were launched at the test site for measuring atmospheric profiles of pressure, temperature and humidity near concurrently with Landsat 7 overpasses. The air temperature at surface level (T_a) and the total column water vapor (W), obtained from the radiosonde profiles are shown in Table II for each case studied. The atmospheric data were used as inputs to the MODTRAN 4 radiative transfer code [7] to calculate the atmospheric transmittance and emitted radiance in the spectral range of the ETM+ thermal band (10.31-12.36 μm). The measured profiles were completed with mid-latitude summer standard

profiles up to 100 km altitude, including the fixed gases. Atmospheric transmittance (τ_λ) and radiance emitted towards the sensor ($L_\lambda^{\uparrow}$) were obtained at nadir. We also calculated the downwelling atmospheric radiance, $L_\lambda^{\downarrow}(\theta)$, at twelve zenith angles from θ=0º to 89º [12], which were used to obtain the hemisphere-integrated downwelling radiance,

$$L_\lambda^{\downarrow} = \frac{1}{\pi} \int_0^{2\pi} \int_0^{\pi/2} L_\lambda^{\downarrow}(\theta) \cos\theta \sin\theta \, d\theta d\varphi \qquad (3)$$

where no dependence on the azimuth angle (φ) is assumed for clear skies and horizontally homogeneous atmospheres.

The spectral radiance measured by the sensor, L_{sen}, can be simulated using the atmospheric transmittance and emitted radiances (forward simulation). For a surface at temperature T and with emissivity ε_λ we can write

$$L_{sen} = \int_0^\infty f(\lambda) \{[\varepsilon_\lambda B_\lambda(T) + (1-\varepsilon_\lambda) L_\lambda^{\downarrow}]\tau_\lambda + L_\lambda^{\uparrow}\} d\lambda \qquad (4)$$

where B_λ is the Planck function for blackbody spectral radiance and $f(\lambda)$ is the normalized spectral response function ($\int_0^\infty f(\lambda) d\lambda = 1$). Lambertian reflection is assumed in (4). The brightness temperature, T_b, corresponding to the simulated at-sensor radiance is calculated using (2). The brightness temperature is usually lower than the true surface temperature (T) in (4) due to atmospheric and emissivity effects.

Equation (4) can also be used to derive the surface temperature T from the satellite-measured at-sensor radiance (inverse simulation). This can be done iteratively by computing the right-hand side integral of (4) for different values of T until the resulting at-sensor radiance matches the satellite-measured L_{sen}. A simpler, approximated approach can be used if the

spectral magnitudes of (4) (B_λ, ε_λ, τ_λ, $L_\lambda^\uparrow$, and $L_\lambda^\downarrow$) are converted to band-averaged magnitudes (B, ε, τ, $L^\uparrow$, and $L^\downarrow$) as

$$B(T) = \int_0^\infty f(\lambda) B_\lambda(T) d\lambda \tag{5}$$

in the case of the Planck function, and analogously for the other spectral magnitudes. Therefore, we can write

$$B(T) = \frac{L_{sen} - L^\uparrow}{\varepsilon \tau} - \frac{1-\varepsilon}{\varepsilon} L^\downarrow \tag{6}$$

from which T can be obtained from the inverted Planck function as in (2), that is

$$T = \frac{k_2}{\ln\left(\frac{k_1}{B(T)} + 1\right)} \tag{7}$$

The error introduced by using (6) with band-averaged magnitudes instead of the spectral integration of (4) increases with the band width, the atmospheric humidity, and the spectral variations of surface emissivity [16]. We compared the surface temperature derived from (6) with that derived from (4) for the ETM+ thermal band and the seven cases studied here. According to the comparison, (6) yielded a small overestimation between 0.15 and 0.3 K in the derived LST. The band-averaged transmittance and atmospheric upwelling and downwelling radiances obtained from the local radiosondes and MODTRAN 4 are listed in Table II.

D. Web-based atmospheric correction tool

Although the Landsat system does not provide an operational LST product, a web-based atmospheric correction tool (ACT) (http://atmcorr.gsfc.nasa.gov) has been developed for single band thermal infrared sensors such as Landsat TM and ETM+ [6]. The tool uses

atmospheric profiles from the National Center for Environmental Prediction (NCEP) [17] as inputs of the MODTRAN 4 radiative transfer code to calculate the atmospheric correction parameters (τ, $L^{\uparrow}$, and $L^{\downarrow}$) for the bandpasses of either the TM or ETM+ thermal bands for a given site and date. With the atmospheric parameters derived from the web-based tool and setting an emissivity value, users can generate their own LST products by applying (6) and (7) for each pixel of the scene.

NCEP atmospheric profiles are available on a 1º×1º longitude/latitude grid every six hours (00:00, 06:00, 12:00, and 18:00 UTC). According to the date and UTC time of the Landsat overpass and the coordinates of the site, the ACT tool retrieves the NCEP profiles for the closest two times (06:00 and 12:00 UTC in our case) and the four surrounding grid locations (39ºN, 0ºE; 39ºN, 1ºW; 40ºN, 0ºE; and 40ºN, 1ºW in our case). Several options are provided to the user for the interpolation of the atmospheric profiles. Option A considers only the grid point closest to the coordinates of the site (39ºN, 0ºE), and the atmospheric profile is generated by linear interpolation between the two times to the given time. Option B uses the four surrounding profiles, which are linearly interpolated to the input location coordinates for each time, and finally the temporal interpolation is performed.

If available, surface atmospheric conditions (altitude, pressure, air temperature and relative humidity) can also be entered in the ACT with either options A and B. In this case, the lower layers of the atmosphere (from 3 km altitude to the surface) are interpolated to remove any discontinuity in the profile. We used the surface conditions measured by the local radiosonde profiles (i. e., at surface altitude z_0=5 m in our case) with both options A and B (hereafter referred to as options A-z_0 and B-z_0, respectively). In this study, we checked the results from the four profile options (Section III.B).

The NCEP interpolated profiles reach an altitude of 30 km, approximately. In the ACT, they are supplemented with standard model atmosphere data (mid-latitude summer in our case) up to 100 km and entered in the MODTRAN 4 code for processing. Finally, the spectral atmospheric transmittance and emitted radiances are band-averaged to obtain τ, $L^{\uparrow}$, and $L^{\downarrow}$ using the specific response function of the sensor. As an example, Table III shows the ETM+ atmospheric parameters obtained for the Valencia test site under option B (spatial interpolation between the four surrounding NCEP profiles) on the seven validation days, together with the air temperature at surface level and the column water vapor obtained from the input profiles.

III. RESULTS AND DISCUSION

A. Landsat 7 Thermal band calibration

In order to validate the radiometric calibration of the ETM+ thermal band, we used the ground-measured temperatures of Table II and the radiosonde profiles to simulate the top-of-atmosphere radiance measured by the sensor, L_{sen}, using (4) (forward simulation). For the surface emissivity, we used the value measured in the field (ε_{λ}=0.983 for all wavelengths). Fig. 1 shows the comparison between the simulated and the satellite-measured at-sensor radiances for the cases analyzed in this study. It appears that the simulated radiances overestimated the satellite radiances especially at the highest values. The mean bias and standard deviation are, respectively, 0.082 and 0.063 $Wm^{-2}sr^{-1}\mu m^{-1}$, with root mean square difference (rmsd) of $\pm$0.104 $Wm^{-2}sr^{-1}\mu m^{-1}$ or $\pm$1.1%.

The comparison was also made in terms of brightness temperatures. Table IV gives the T_b values corresponding to the simulated L_{sen} and the differences with the satellite brightness

temperatures of Table I (δT_b). Fig. 2 plots the brightness temperature difference δT_b as a function of the simulated T_b, showing the underestimation of satellite T_b for the higher temperatures, as mentioned above. In Table IV, differences ranged between -0.2 and 1.1 K, with mean bias of 0.6 K and standard deviation of 0.5 K (rmsd=±0.8 K). These results are close to the ±0.6 K uncertainty reported in [2] and [5]. Although the validation data are few and correspond to a narrow range of conditions (full vegetated surface, T_b from 22 to 25 ºC, T_g from 27 to 29 ºC, W from 2 to 3 cm, T_a from 24 to 32 ºC), the results shown here indicate that the ETM+ thermal band continues to provide a good accuracy.

We performed an uncertainty analysis for the brightness temperatures simulated with (4). We considered the uncertainty of the ground LST and emissivity measurements, errors in the atmospheric profiles, and the uncertainty in the radiative transfer model. Data for case 4 of Table II were used in the calculations, since it is representative of the overall conditions of the study. For an error of 0.6 K in the ground LST, the error in the simulated T_b is 0.4 K. The uncertainty in the measured emissivity is 0.005, which results in an error of 0.12 K in T_b. Following [3], errors in atmospheric profiles were simulated in two ways. First, the water vapor mixing ratio was increased by 10% at each profile level (i.e., an increase of 0.25 cm in column water vapor for case 4). Second, the air temperature was increased by 1 K at each level. These changes correspond to the reported accuracy of the radiosonde measurement, and can also be regarded as small temporal and spatial variations in the atmosphere. For each case, T_b was calculated and compared with the value obtained with the original profile. Differences (in absolute value) were 0.14 K for the water vapor variation and 0.4 K for the temperature variation. The total atmospheric error in T_b was calculated as the root sum squares (RSS) of the above values (0.4 K).

The accuracy of the MODTRAN 4 code in the TIR region is addressed in [18], showing biases at 12 μm due to uncertainties in the water vapor continuum absorption. We assumed that the uncertainty in the MODTRAN calculations is equal to the total atmospheric error. Finally, the total uncertainty in the simulated T_b is obtained as the RSS of the above errors, yielding ±0.7 K. The largest part of the error is due to the atmospheric variations and the radiative transfer uncertainty. The error is compatible with the δT_b differences of Table IV.

B. LST retrieval from Landsat 7 data

Equation (6) was used for LST retrieval from the satellite-measured at-sensor radiances (inverse simulation). For the atmospheric parameters τ, $L^{\uparrow}$, and $L^{\downarrow}$, we employed: (1) the values obtained from the local radiosonde profiles given in Table II, and (2) the values provided by the ACT described in Section II.D. In both cases, we used the same surface emissivity (ε=0.983), and the resulting LSTs were compared with the ground-measured LSTs of Table II.

The LST values obtained from the local atmospheric parameters are shown in Table IV, together with the differences between the ground and satellite-derived LSTs (δT). LST differences were usually slightly larger than the corresponding differences in the brightness temperatures (δT_b), as expected when comparing inverse and forward simulations. δT ranged between -0.6 and 1.4 K, with mean bias of 0.7 K, standard deviation of 0.7 K and rmsd=±1.0 K. These results compare well with those reported in [19] over agricultural fields using ETM+ data acquired in 2002 (rmsd=±1.2 K for Landsat 7, with satellite LSTs usually underestimating the ground LSTs). In situ measurements were used in [20] for evaluating lake surface temperatures retrieved from Landast 7 data acquired in 2000, with rmsd of ±1.4 K.

We performed an uncertainty analysis of the LST derivation from (6). As in section III.A, validation case 4 was used for the calculations. For the inverse simulation, we considered the uncertainty in the ETM+ calibration (0.6 K in T_b), the emissivity uncertainty (0.005), and the errors in the atmospheric profiles and radiative transfer model, which were simulated as in Section III.A. We also included the error due to the approximation of (6) (<0.3 K, section II.C). The resulting RSS error was ±1.2 K, with the largest parts corresponding to the calibration error and the atmospheric correction uncertainties. The error is compatible with the δT differences of Table IV.

Table V shows the differences between the ground and the satellite LSTs obtained from the operational ACT with the four profile options (A, B, A-z_0 and B-z_0) described in section II.D. The best overall results were obtained with option B (spatially interpolated profiles), with differences ranging from -1.8 to 1.3 K, with zero average bias, standard deviation of 1.1 K and rmsd=±1.1 K. Option A (closest grid profile) yielded mostly similar results, with the only exception of case 7 where δT changed by 2 K. The mean bias was -0.4 K (satellite LSTs overestimating ground LSTs), with standard deviation of 1.0 K and rmsd=±1.1 K. On the other hand, options A-z_0 and B-z_0 (using measured atmospheric variables at surface level) provided similar results for most of the cases, except for validation case 4 where the satellite LST overestimated the ground LST by 3-4 K, thus increasing the rmsd to ±1.7 K in both options. If case 4 was excluded, option B-z_0 would yield rmsd of ±0.7 K.

The results obtained with option B compare well with those obtained from the local radiosonde profiles. Fig. 3 shows the ground measured LSTs against the satellite-derived LSTs from both the radiosonde profiles and the ACT tool. Most of the validation cases in Fig. 3 agree with the 1:1 line within the LST uncertainty limits. The larger dispersion in the ACT

cases is apparent, as well as the LST underestimation yielded by the radiosondes (average bias of 0.7 K). In principle, local radiosonde profiles measured near-concurrently with the satellite overpass should provide the best estimate of the atmospheric state over the test site and thus the best atmospheric correction for at-sensor radiances. However, radiosonde measurements are usually limited to validation campaigns and cannot be used for operational LST derivation. The results shown here demonstrate that the web-based ACT relying on NCEP profiles may provide accurate LST estimates. It should be noted that the atmospheric water vapor was relatively high in all the validation cases (2.2-3.6 cm), i.e., when the ACT is expected to be less accurate [6].

Differences in the LSTs retrieved from local radiosondes and ACT are due to differences in the atmospheric temperature and water vapor profiles used as inputs of the MODTRAN 4 code. As an example, Fig. 4 shows a comparison between the radiosonde and NCEP profiles (options B and B-z_0) for validation case 4. For this case, option B overestimated the radiosonde LST by 1.1, whereas it was the worst case for option B-z_0 with an overestimation of 4.6 K. As seen in Fig. 4a, NCEP and radiosonde air temperatures show differences of a few degrees in the layers below 1 km and agreed quite well above that height. However, the NCEP profile modified with surface data did not provide a better agreement since the ACT interpolates the lower layers from surface level up to 3 km [6], which appears inadequate for the cases studied here. With regard to the water vapor mixing ratio (Fig. 4b), the NCEP profiles usually yielded larger values than the radiosonde profiles. Accordingly, NCEP overestimated column water vapor by 0.4 cm in average and up to 0.7 cm in cases 4 and 5 (Tables II and III). On the other hand, the surface level of the NCEP profiles were between 130 and 350 m above the test site (z_0=5 m), thus the lowest layer of the atmosphere with

typically the largest water vapor content and warmest temperature was neglected in the ACT calculations.

As seen in Fig. 5a, the LST difference between the two profiles shows certain correlation with the column water vapor difference, with LSTs from ACT usually overestimating the radiosonde-based LSTs (average bias of 0.7 K, rmsd=±1.2 K) and the largest difference corresponding to case 5 (2.2 K). However, the differences in retrieved LSTs cannot be fully explained by the differences in column water vapor alone, but they are related to differences in the atmospheric parameters τ and $L^{\uparrow}$ used in (6). Note that the impact of $L^{\downarrow}$ is much smaller since the emissivity assumed in (6) is high and we took the same value for both the ACT and radiosonde-based LST retrieval. In order to assess the impact of τ and $L^{\uparrow}$ in the LST retrieval, we used an expression for the atmospheric correction, ΔT_{atm} (i.e., the term to be added to at-sensor brightness temperatures, T_b, to compensate for the atmospheric absorption and emission) derived in [21], that is

$$\Delta T_{atm} = \frac{1-\tau}{\tau}(T_b - T_{eff}) \tag{8}$$

where T_{eff} is the effective atmospheric temperature, which represents the average temperature of the atmosphere in terms of the emitted radiance and is defined from the atmospheric transmittance and upwelling radiance as

$$L^{\uparrow} = (1-\tau)\, B(T_{eff}) \tag{9}$$

from which T_{eff} can be inverted as in (7). Since water vapor is the main absorber and emitter in the thermal band, T_{eff} can be regarded as the average atmospheric temperature weighted by the water vapor mixing ratio profile, so T_{eff} is usually close to the air temperature at low levels (~2 km).

According to (8), the atmospheric correction depends on both the transmittance factor TF=(1-τ)/τ, and the difference between the brightness temperature and the effective atmospheric temperature. Table VI shows TF and T_{eff} as obtained from the radiosonde profiles and the ACT, option B. It should be noted that ACT yielded lower TF values (higher τ) than radiosonde profiles for cases 1, 2 and 7 despite higher values of column water vapor (see Tables II and III). This is because atmospheric transmittance is not only determined by column water vapor, but also by the vertical distribution of water vapor and temperature due to the temperature dependence of the water vapor continuum absorption [22]. Fig. 5b shows that the differences between ACT and radiosonde-derived LSTs are well correlated with the difference in the transmittance factor, as opposed to the lower correlation with the difference in column water vapor shown in Fig. 5a.

In Table VI, T_{eff} is usually 1-2 K colder for ACT than for radiosondes because the lower, warmer atmospheric layer missing in the NCEP profiles, thus implying an overestimation of 0.5-1 K on the ACT-retrieved LST. This is superimposed to the effect of the differences in TF, which were of both signs as discussed above. Consequently, the ACT-derived LSTs generally overestimated the radiosonde-derived LSTs in the cases analyzed here. These results show the high sensitivity of the derived LST to the water vapor and temperature profiles, which are both necessary for calculating the atmospheric parameters τ and $L^{\uparrow}$.

IV. CONCLUSIONS

The ETM+ thermal band calibration and the atmospheric correction tool available at http://atmcorr.gsfc.nasa.gov were validated with ground measurements performed over rice fields for seven cases in the summers of 2004-2007. Using the ground-measured LST and emissivity, and the temperature and water vapor profiles provided by local radiosondes, the

at-sensor radiances and equivalent brightness temperatures were calculated by means of the MODTRAN 4 code [7]. The comparison with satellite radiances and brightness temperatures showed rmsd of ±0.104 $Wm^{-2}sr^{-1}\mu m^{-1}$ (±1.1%) and ±0.8 K, respectively. These results agree well with previous ETM+ vicarious calibration studies ([1], [2] and [5]).

LSTs derived from at-sensor ETM+ radiances using the web-based ACT [6] showed a good agreement with the ground-measured LSTs, with differences within the ±1 K range for most of the cases. The best overall results (rmsd=±1.1 K and zero average bias) were obtained for the option using atmospheric profiles interpolated from the four nearest NCEP grids. The ACT-derived LSTs were also compared with LSTs obtained using local radiosonde profiles, which likely represent ideal conditions for atmospheric correction. The differences yielded rmsd=±1.2 K, with ACT overestimating the radiosonde LSTs by 0.7 K in average. Such differences were analyzed in terms of the atmospheric correction parameters showing the high sensitivity to the temperature and water vapor profiles. It should be noted that, for all the validation cases studied here, the column water vapor was relatively high (>2 cm) and thus the ACT accuracy is expected to be lower [6].

The results shown here confirm the good quality of the ETM+ thermal data and that the operational, web-based ACT relying on NCEP profiles may provide LST estimates within an accuracy of ±1 K. However, the limited number of validation cases and conditions of the study (one landcover at morning and summer) prevents the generalization of the results for other cases such as cold weather situations or high column water vapor (W>3 cm). The test site used here (full-cover rice fields) is a homogeneous and high-emissivity surface, thus easing the emissivity correction for LST derivation. Other targets such as bare surfaces and semi-arid areas may have lower emissivities (hence increasing the impact of reflected

downwelling sky irradiance), with larger variability and uncertainty. For these cases, the emissivity correction may be affected by a larger error and the derived LSTs may be less accurate than in the present case.

ACKNOWLEDGMENTS

This work was funded by the Spanish *Ministerio de Educación y Ciencia* (Projects CGL2004-06099-C03-01 and CGL2007-64666/CLI, co-financed with European Union FEDER funds, *Acción Complementaria* CGL2007-29819-E, and research grant of J. M. Galve), and *Ministerio de Ciencia e Innovación* ("*Juan de la Cierva*" research contract of J. M. Sánchez). Landsat 7 ETM+ data were provided by United States Geological Survey EROS Data Center. We thank the Thermal Remote Sensing group of the University of Valencia for the ground LST and emissivity measurements and Centro de Estudios Ambientales del Mediterraneo (CEAM) for the radiosonde data.

REFERENCES

[1] J. R. Schott, J. A. Barsi, B. L. Nordgren, N. G. Raqueno, and D. de Alwis, "Calibration of Landsat thermal data and application to water resource studies," *Remote Sensing of Environment*, vol. 78, pp. 108-117, 2001.

[2] J. A. Barsi, J.R. Schott, F.D. Palluconi, D.L. Helder, S.J. Hook, B.L., Markham, G. Chander, E.M. O'Donnell, "Landsat TM and ETM+ Thermal Band Calibration," *Canadian Journal of Remote Sensing*, vol. 28, no. 2, pp. 141-153, 2003.

[3] S. J. Hook, G. Chander, J. A. Barsi, R. E. Alley, A. Abtahi, F. D. Palluconi, B. L. Markham, R. C. Richards, S. G. Schladow, and D. L. Helder, "In-flight validation and recovery of water surface temperature with Landsat-5 thermal infrared data using an automated high-altitude lake validation site at Lake Tahoe," *IEEE Transactions on Geoscience and Remote Sensing*, vol. 42, no. 12, pp. 2767-2776, Dec. 2004.

[4] J. A. Barsi, S. J. Hook, J. R. Schott, N. G. Raqueno, and B. L. Markham, "Landsat-5 Thematic Mapper Thermal Band Calibration Update," *IEEE Geoscience and Remote Sensing Letters*, vol. 4, no. 4, pp. 552-555, Oct. 2007.

[5] J. A. Barsi, B. L. Markham, D. L. Helder, and G. Chander, "Radiometric calibration status of Landsat-7 and Landsat-5," *Sensor, Systems and Next-Generation Satellites. Proceedings of SPIE*, vol. 6744, pp. 67441F, 2007.

[6] J. A. Barsi, J. R. Schott, F. D. Palluconi, and S. J. Hook, "Validation of a web-based atmospheric correction tool for single thermal band instruments," *Proceedings of SPIE Vol. 5882*, doi: 10.1117/12.619990, 2005.

[7] A. Berk, G. P. Anderson, P. K. Acharya, J. H. Chetwynd, L. S. Bernstein, E. P. Shettle, M. W. Matthew, and S. M. Adler-Golden, "MODTRAN 4 user's manual," Air Force Research Laboratory, Space Vehicles Directorate, Air Force Materiel Command, Hascom AFB, MA, 95 pp., 1999.

[8] B. L.Markham, J. C. Storey, D. L. Williams, and J. R. Irons, "Landsat sensor performance: History and current status," *IEEE Transactions on Geoscience and Remote Sensing*, vol. 42, no. 12, pp. 2691-2694, Dec. 2004.

[9] C. Coll, V. Caselles, J. M. Galve, E. Valor, R. Niclòs, J. M. Sánchez, and R. Rivas, "Ground measurements for the validation of land surface temperatures derived from AATSR and MODIS data," *Remote Sensing of Environ*ment, vol. 97, pp. 288-300, 2005.

[10] C. Coll, V. Caselles, J. M. Galve, E. Valor, R. Niclòs, and J. M. Sánchez, "Evaluation of split-window and dual-angle correction methods for land surface temperature retrieval from Envisat/AATSR data," *Journal of Geophysical Research,* vol. 111**,** 12105, doi 10.1029/ 2005JD006830, 2006.

[11] C. Coll, V. Caselles, E. Valor, R. Niclòs, J.M. Sánchez, J.M. Galve, and M. Mira, "Temperature and emissivity separation from ASTER data for low spectral contrast surfaces," *Remote Sensing of Environment*, vol. 110, pp. 162-175, 2007.

[12] J. M. Galve, C. Coll, V. Caselles and E. Valor, "An Atmospheric Radiosounding database for generating Land Surface Temperature algorithms," *IEEE Trans. Geosci. Remote Sens.*, vol. 46, no. 5, pp. 1547-1557, May 2008.

[13] C. Coll, S. J. Hook, and J. M. Galve, "Land surface temperature from the Advanced Along-Track Scanning Radiometer: Validation over inland waters and vegetated surfaces," *IEEE Trans. Geosci. Remote Sens.*, vol. 47, no. 1, pp. 350-360, Jan 2009.

[14] M. Sicard, P. R. Spyak, G. Brogniez, M. Legrand, N. K. Abuhassan, C. Pietras, and J. P. Buis, "Thermal infrared field radiometer for vicarious cross-calibration: characterization and comparisons with other field instruments," *Optical Engineering*, vol. 38, no. 2, pp. 345-356, 1999.

[15] E. Rubio, V. Caselles, C. Coll, E. Valor, and F. Sospedra, "Thermal-infrared emissivities of natural surfaces: Improvements on the experimental set-up and new measurements," *International Journal of Remote Sensing*, vol. 24, no. 24, pp. 5379-5390, 2003.

[16] R. Richter, and C. Coll, "Band-pass resampling effects for the retrieval of surface emissivity," *Applied Optics*, vol. 41, no. 18, pp. 3523-3529, 2002.

[17] E. Kalnay, M. Kanamitsu, R. Kistler, W. Collins, D. Deaven, L. Gandin, M. Iredell, S. Saha, G. White, J.Woollen, Y. Zhu, M. Chelliah, W. Ebissuzaki, W. Higgins, J. Janowiak, K.C. Mo, C. Ropelewski, J. Wang, A. Leetmaa, R. Reynolds, R. Jenne and D. Joseph. "The NCEP/NCAR 40 Year Reanalysis Project. *Bulletin of the American Meteorological Society*," vol. 77, pp. 437-471, 1995.

[18] P. Dash, and A. Ignatov, "Validation of clear-sky radiances over oceans simulated with MODTRAN4.2 and global NCEP GDAS fields against nighttime NOAA15-18 and MetOp-A AVHRR data," *Remote Sensing of Environment*, vol. 112, pp. 3012-3029, 2008

[19] F. Li, T. J. Jackson, W. P. Kustas, T. J. Schmugge, A. N. French, M. H. Cosh, and R. Bindlish, "Deriving land surface temperature from Landsat 5 and 7 during SMEX02/SMACEX," *Remote Sensing of Environment*, vol. 92, pp. 521-534, 2004.

[20] C. Wloczyk, R. Richter, E. Borg, W. Neubert, "Sea and lake surface temperature retrieval from Landsat thermal data in Northern Germany," *International Journal of Remote Sensing*, vol. 27, no. 12, pp. 2489-2502, 2006.

[21] C. Coll, V. Caselles, J. A. Sobrino, and E. Valor, "On the atmospheric dependence of the split-window equation for land surface temperature," *International Journal of Remote Sensing*, vol. 15, no. 1, pp. 105-122, 1994.

[22] A.N. French, J.M. Norman, M.C. Anderson, “A simple and fast atmospheric correction for spaceborne remote sensing of surface temperature.” *Remote Sensing of Environment*, vol. 87, pp. 326–333, 2003.

TABLES

Table I. Date and time of the Landsat 7 scenes used in this study. T_b is the brightness temperature for the valid pixel closest to the test site.

Case	Date	UTC Time (h:m)	path/row	Processing Level	T_b (ºC)
1	August 12, 2004	10:26	198/33	L1G	24.9
2	July 21, 2005	10:33	199/33	L1T	24.4
3	August 6, 2005	10:33	199/33	L1T	24.4
4	July 24, 2006	10:33	199/33	L1T	24.9
5	August 2, 2006	10:27	198/33	L1G	23.9
6	July 11, 2007	10:34	199/33	L1T	21.8
7	July 20, 2007	10:27	198/33	L1G	22.8

Table II. Ground-measured LSTs (T_g) and uncertainties (σ) concurrent to Landsat 7 overpasses. T_a is the air temperature at surface level and W is the column water vapor from the local radiosondes. The atmospheric transmittance (τ), upwelling radiance ($L^{\uparrow}$) and downwelling radiance ($L^{\downarrow}$) calculated from the radiosondes and MODTRAN 4 are also given.

Case	T_g (ºC)	σ (K)	T_a (ºC)	W (cm)	τ	$L^{\uparrow}$ ($Wm^{-2}sr^{-1}\mu m^{-1}$)	$L^{\downarrow}$ ($Wm^{-2}sr^{-1}\mu m^{-1}$)
1	28.2	0.6	32.0	2.09	0.72	2.36	4.25
2	28.1	0.4	27.2	2.01	0.71	2.44	4.27
3	28.1	0.5	27.8	1.86	0.78	1.86	3.46
4	28.8	0.4	28.0	2.39	0.66	2.86	4.89
5	29.0	0.9	28.6	2.86	0.61	3.21	5.34
6	26.9	0.5	24.4	2.90	0.59	3.16	5.20
7	28.0	0.4	26.6	2.90	0.56	3.56	5.72

Table III. Atmospheric parameters from the web-based atmospheric correction tool (ACT) using spatial interpolation between the four closest NCEP profiles (option B). T_a is the air temperature at surface level, W is the column water vapor, τ is the transmittance, $L^{\uparrow}$ is the upwelling radiance, and $L^{\downarrow}$ is the downwelling radiance.

Case	T_a (ºC)	W (cm)	τ	$L^{\uparrow}$ ($Wm^{-2}sr^{-1}\mu m^{-1}$)	$L^{\downarrow}$ ($Wm^{-2}sr^{-1}\mu m^{-1}$)
1	27.6	2.15	0.76	1.93	3.13
2	26.7	2.47	0.72	2.37	3.76
3	27.2	2.34	0.75	2.02	3.27
4	28.0	3.07	0.65	2.86	4.5
5	26.1	3.59	0.52	3.93	5.82
6	22.1	3.04	0.59	3.08	4.69
7	25.5	2.91	0.63	2.99	4.61

Table IV. Simulated brightness temperatures using the local radiosondes profiles (T_b) and difference between simulated and satellite-measured brightness temperatures (δT_b). LSTs derived from satellite data and local radiosonde profiles (T) and difference between ground and satellite-derived LSTs (δT).

Case	T_b (ºC)	δT_b (K)	T (ºC)	δT (K)
1	25.2	0.3	28.0	0.2
2	25.3	1.0	26.9	1.2
3	25.5	1.1	26.8	1.3
4	25.4	0.6	28.2	0.6
5	24.9	1.0	27.6	1.4
6	21.6	-0.2	27.5	-0.6
7	23.4	0.5	27.4	0.6

Table V. Differences between ground and satellite LST (δT) for the ACT with the four options A, B, A-z_0 and B-z_0 (see text for details).

	δT (K)			
Case	**A**	**B**	**A-z_0**	**B-z_0**
1	0.2	0.0	1.8	1.2
2	1.1	1.3	-0.2	-0.7
3	0.3	0.5	0.7	0.5
4	-0.4	-0.5	-3.2	-4.0
5	-0.7	-0.8	1.2	0.3
6	-2.1	-1.8	1.6	0.7
7	-0.9	1.1	-0.2	-0.2

Table VI. Transmittance factor TF=(1-τ)/τ and atmospheric effective temperature T_{eff} calculated from the radiosonde profiles and ACT, option B.

	radiosonde		ACT (B)	
Case	**TF**	**T_{eff} (ºC)**	**TF**	**T_{eff} (ºC)**
1	0.397	18.4	0.316	16.5
2	0.408	19.5	0.389	19.8
3	0.290	18.2	0.333	16.8
4	0.516	19.4	0.538	17.5
5	0.631	18.6	0.923	17.6
6	0.691	13.9	0.695	12.1
7	0.775	17.3	0.587	16.8

FIGURE CAPTIONS

Fig. 1. Comparison between simulated and satellite at-sensor radiances. The linear regression is shown. Case number is displayed next to each data point.

Fig. 2. Difference between simulated and satellite brightness temperatures against the simulated brightness temperatures. Case number is displayed next to each data point.

Fig. 3. Comparison between ground-measured LSTs and satellite LSTs derived with local radiosonde profiles (closed circles) and the atmospheric correction tool, option B (open circles). The error bars for both ground-measured and satellite-derived LSTs are shown.

Fig. 4. Atmospheric profiles from local radiosonde, ACT-option B and ACT-option B modified with surface data for validation case 4 (July 24, 2006). (a) Air temperature. (b) Water vapor mixing ratio.

Fig. 5. Difference between LSTs derived from ACT, option B and local radiosonde profiles against (a) column water vapor (W) difference, and (b) transmittance factor ($TF=(1-\tau)/\tau$) difference. Case number is displayed next to each data point.

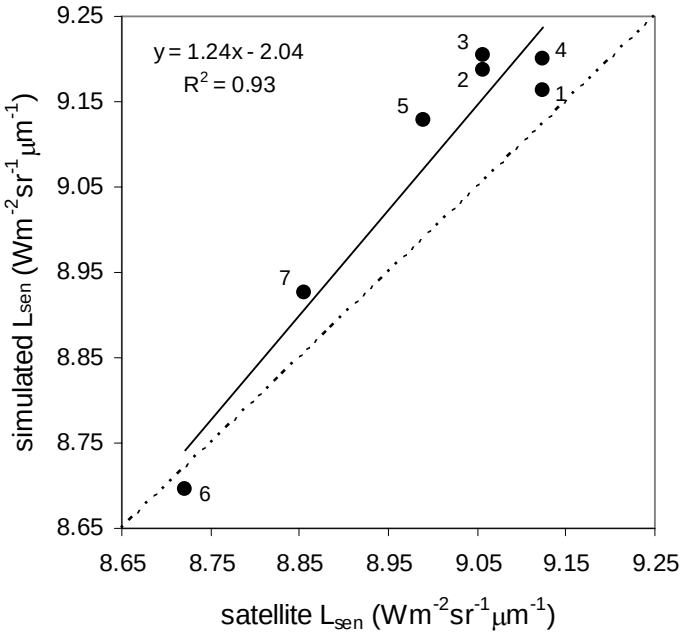
y = 1.24x - 2.04
R2 = 0.93
simulated Lsen (Wm-2sr-1μm-1)
satellite Lsen (Wm-2sr-1μm-1)
9.25
9.15
9.05
8.95
8.85
8.75
8.65
8.65
8.75
8.85
8.95
9.05
9.15
9.25
1
2
3
4
5
6
7

Figure 1

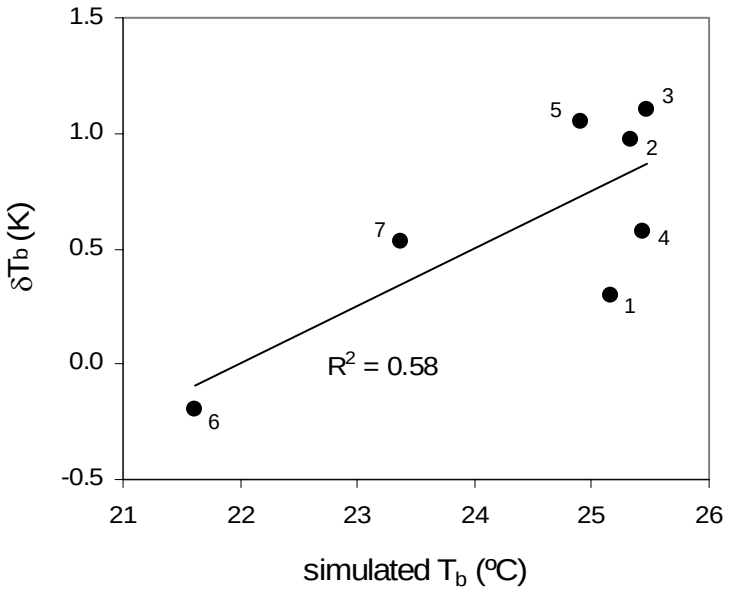
1.5
1.0
0.5
0.0
-0.5
δTb (K)
21
22
23
24
25
26
simulated Tb (ºC)
R2 = 0.58
1
2
3
4
5
6
7

Figure 2

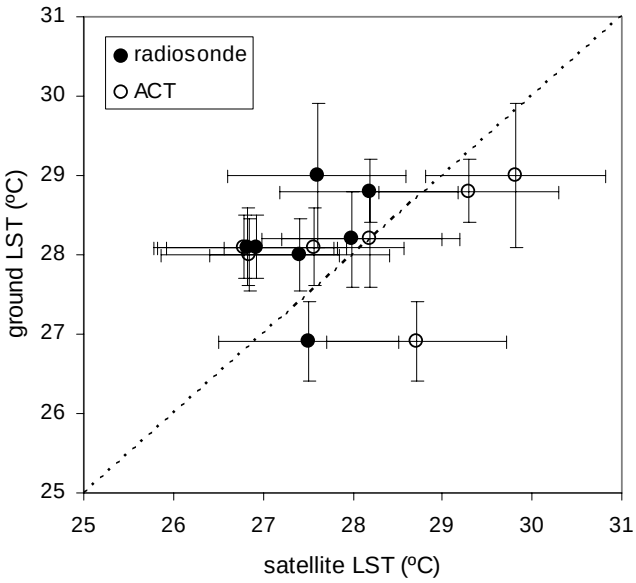
radiosonde
ACT
ground LST (ºC)
satellite LST (ºC)
31
30
29
28
27
26
25
25
26
27
28
29
30
31

Figure 3

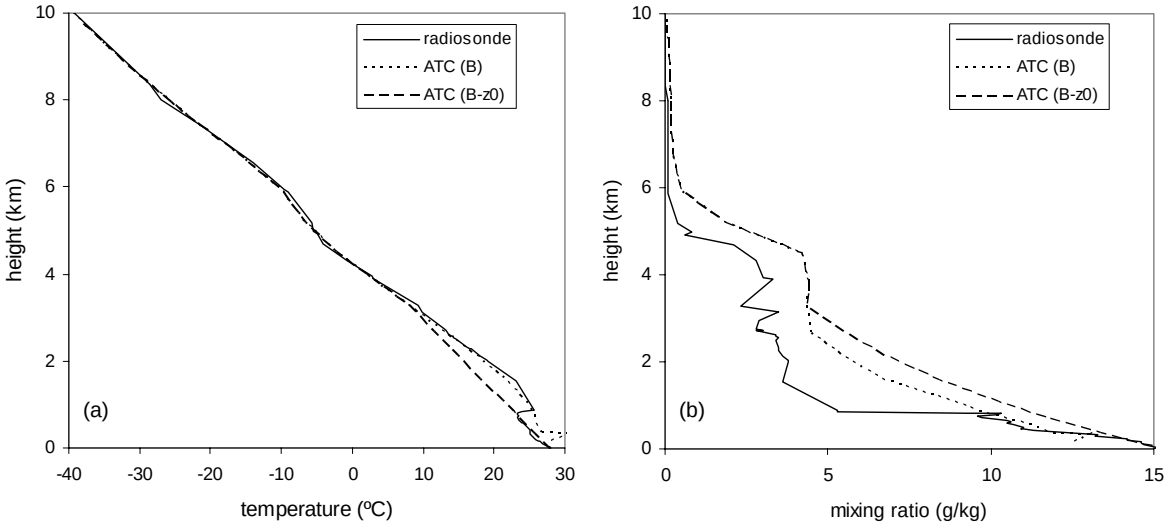
radiosonde
ATC (B)
ATC (B-z0)
height (km)
temperature (ºC)
(a)
mixing ratio (g/kg)
(b)

Figure 4

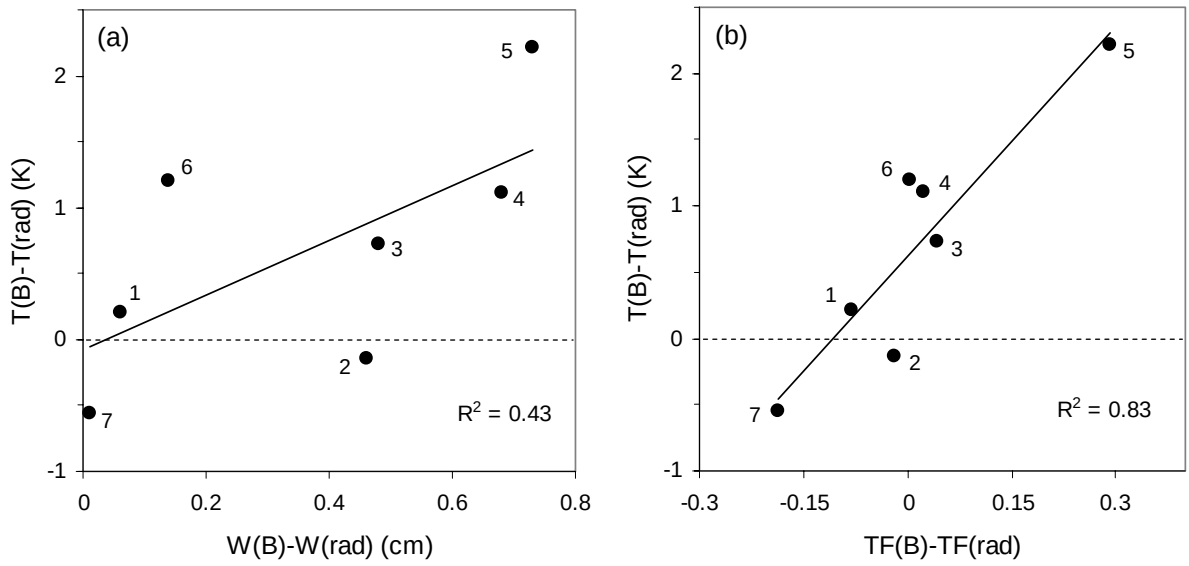

Figure 5